

Chapter 5

TWO-DIMENSIONAL BLADE-TO-BLADE FLOW THROUGH CASCADES OF BLADES

Prediction of the flow through cascades of blades is fundamental to all aspects of axial-flow compressor aerodynamic design and analysis. Although the flow through the annular cascades of blades in a compressor is really a three-dimensional flow problem, there are many advantages to considering the simpler problem of two-dimensional flow in cascades. It offers a very natural view of cascade fluid dynamics to make it easier for designers to develop an understanding of the basic flow processes involved. Indeed, very simple two-dimensional cascade flow models were used in this educational role long before computational methods and computers had evolved enough to produce useful design results. Today, blade-to-blade flow analysis is a useful design and analysis tool that provides reasonable approximations to many problems of interest. Inviscid blade-to-blade flow analysis addresses the general problem of two-dimensional flow on a stream surface in an annular cascade, as discussed in Chapter 3. Two-dimensional boundary layer analysis can be used to approximate viscous effects. Although very useful, this approach does have limitations. It ignores secondary flows that develop from the migration of low momentum boundary layer fluid across the stream sheet. It also loses accuracy when significant flow separation is present. This chapter considers theoretical methods to model two-dimensional blade-to-blade flow. The next chapter considers a different approach to the problem, where empirical models are derived from two-dimensional cascade test data. The methods presented in this chapter are basically the same as those presented in Aungier (2000), but are adapted to conventions more commonly used for axial-flow compressors. Aungier (2000) provides detailed guidance relative to implementation of the methods in numerical analyses that is not repeated here. Readers interested in those details should consult the original reference.

NOMENCLATURE

- A = area and a function used in Eq. (5-22)
- a = sound speed and a parameter in Eq. (5-52)

- B = function in Eq. (5-23)
 b = stream sheet thickness
 C = absolute velocity and a function in Eq. (5-24)
 c_f = skin friction coefficient
 c_p = specific heat at constant pressure
 D = function in Eq. (5-25)
 E = function in Eq. (5-26) and the entrainment function
 \vec{n} = a unit vector
 H = total enthalpy and shape factor of Eq. (5-129)
 H_k = kinematic shape factor, Eq. (5-130)
 H_l = shape factor, Eq. (5-128)
 h = enthalpy
 I = rothalpy
 K = shape factor of Eq. (5-122)
 M = Mach number = C/a
 m = meridional coordinate
 \dot{m} = mass flow rate
 \vec{r} = unit vector normal to an area element
 P = pressure
 Q = velocity component of Eq. (5-76)
 Re_θ = momentum thickness Reynolds number
 r = radius
 S = blade pitch = $r (\theta_l - \theta_0)$
 T = temperature
 t = time
 u = general function
 V = volume
 v = general function
 W = relative velocity
 x = distance along a wall
 y = distance normal to a wall
 z = axial coordinate
 α = angle of attack = $\beta_m - \gamma$
 β = flow angle and coordinate angle (Fig 5-4)
 γ = blade stagger angle
 δ = boundary layer thickness
 δ' = density thickness
 δ^* = displacement thickness
 δ_E = energy thickness
 δ_h = enthalpy thickness
 δ_u = velocity thickness
 η = dimensionless tangential coordinate (Fig. 5-3)
 θ = polar angle and momentum thickness
 Λ = shape factor of Eq. (5-113)
 μ = stabilizing term and viscosity
 ξ = streamwise coordinate (Fig. 5-3)
 ρ = density
 Φ = stabilizing term

- ϕ = stream surface slope angle with axis
 ψ = stream function
 τ_w = wall shear stress
 ω = rotation speed
 $\bar{\omega}$ = total pressure loss coefficient

Subscripts

- in = cascade inlet condition
 m = meridional component
 out = cascade discharge condition
 q = component normal to ξ coordinate
 t = total thermodynamic condition
 θ = tangential component
 ξ = component tangent to ξ coordinate
 0 = parameter on blade surface θ_0 (Fig. 5-3)
 1 = parameter on blade surface θ_1 (Fig. 5-3)

Superscripts

- (η) = relative to the η direction
 (ξ) = relative to the ξ direction
 $'$ = relative condition and first derivative
 $''$ = second derivative

5.1 THE BLADE-TO-BLADE FLOW PROBLEM

Figures 5-1 and 5-2 illustrate the basic problem to be considered. Figure 5-1 shows a schematic of a streamline pattern on a stream sheet between adjacent blades in a cascade of blades. It will be sufficient to consider a single passage between two blades, since the flow in all blade passages will be assumed to be identical. As discussed in Chapter 3, a stream sheet is a thin annular passage bounded by two stream surfaces, where a stream surface has no velocity component normal to it, i.e., it has no mass flow across it. A schematic of a stream sheet that might be used is illustrated in Fig. 5-2. Stream sheets will be assumed to be axisymmetric. Although that is not a necessary assumption, it does greatly simplify the problem. This chapter considers the stream sheet geometry to be known. In later chapters, techniques to define the stream sheet geometry to support these blade-to-blade flow methods will be covered, including generalization of the process into a quasi-three-dimensional flow analysis.

The approach to be used is to generate a time-steady inviscid flow analysis followed by a blade surface boundary layer analysis to approximate viscous effects. It is assumed that the rothalpy and entropy are both constant at the upstream boundary. From the time-steady form of Eqs. (3-25), (3-28) and (3-29), it can be

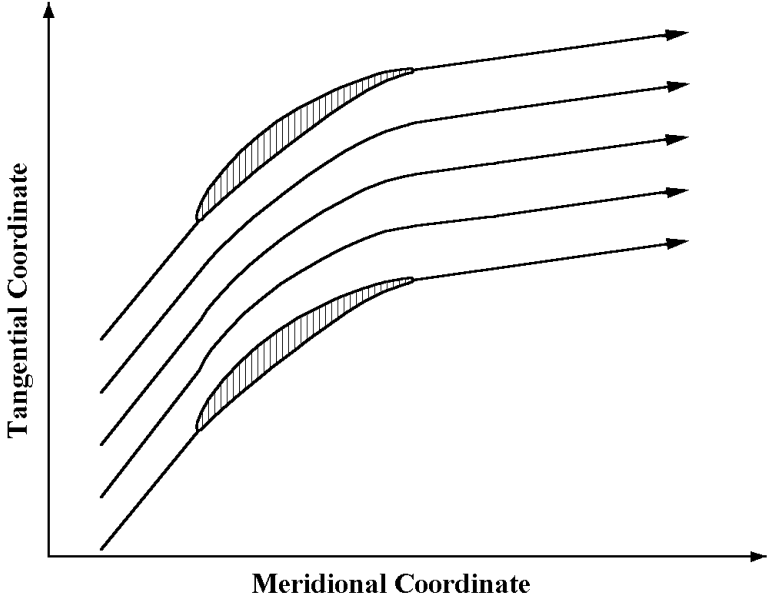


FIGURE 5-1 Blade-to-Blade Plane Flow

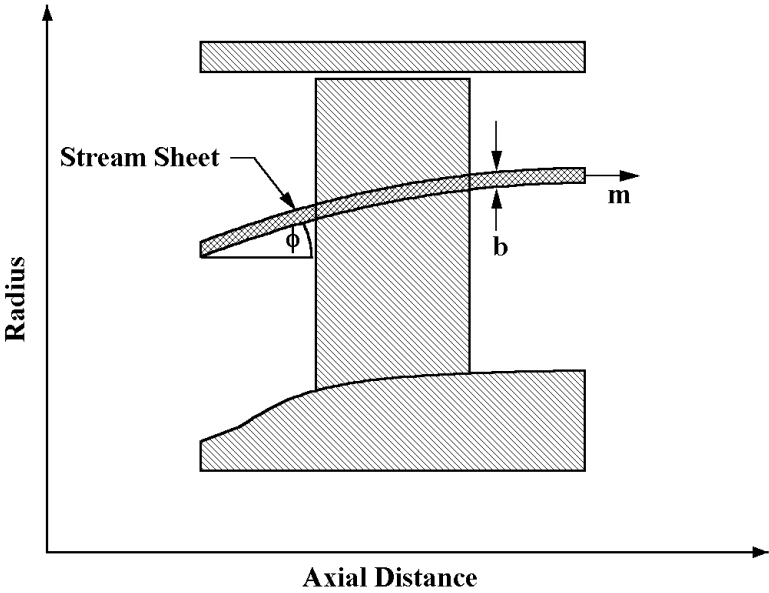


FIGURE 5-2 Blade-to-Blade Stream Sheet

seen that these assumptions require rothalpy and entropy to be constant over the entire stream sheet. The steady form of Eqs. (3-28) and (3-29) governs conservation of momentum in the stream sheet. It is seen that these two equations are identical for the present problem. Indeed, from Eqs. (3-1), (3-29) and (3-63) it is easily shown that the component of the absolute vorticity normal to the stream sheet must be zero. This reduces the problem to a classical potential flow problem governed by conservation of mass, Eq. (3-21), and the irrotational flow condition, Eq. (3-29).

But a major complication encountered in blade-to-blade flow analysis arises from the mathematical character of the governing equations of motion for time-steady inviscid flow. When the flow is everywhere subsonic ($W < a$), the governing equations are elliptic in form. This presents a classical boundary value problem, where the solution is completely determined by conditions imposed on the boundaries of the solution domain. But when the flow is supersonic ($W > a$), the governing equations are hyperbolic in form. This type of problem requires some type of marching solution, such as the method of characteristics. When supersonic flow is present, there is usually subsonic flow present in the solution domain. The mixed subsonic-supersonic flow problem requires two solution techniques that must be matched in some fashion. It is now common practice to consider time-unsteady flow in those cases, since the governing equations for unsteady inviscid flow are hyperbolic for both subsonic and supersonic flow. This solution technique is commonly called the time-marching or time-dependent technique. The solution is simply advanced in time until it has reached essentially a steady flow prediction. When the time-marching approach is used, the simplifications that lead to the potential flow model are no longer present. For example, Eq. (3-25) must be solved, since rothalpy can no longer be treated as a constant on the stream sheet. Nor are the two momentum equations for the flow in the stream sheet identical for the time-unsteady case. Thus, a potential flow analysis can be used for subsonic flow, but a more general analysis will be needed for a mixed subsonic-supersonic flow case. These more general solutions are commonly referred to as Euler techniques, which include the time-marching method. The basic characteristic of an Euler method is that conservation of mass, energy and all relevant momentum equations are solved without simplification, such as assuming isentropic flow.

5.2 COORDINATE SYSTEM AND VELOCITY COMPONENTS

Figure 5-3 illustrates the solution domain to be considered for the blade-to-blade flow solution. It is convenient to use a coordinate transformation to define new coordinates (ξ, η) such that the blade surfaces correspond to lines of constant η . The new coordinates are given by

$$\xi = \int_0^m \frac{dm}{\cos \beta} \quad (5-1)$$

$$\eta = [\theta - \theta_0] / [\theta_1 - \theta_0] \quad (5-2)$$

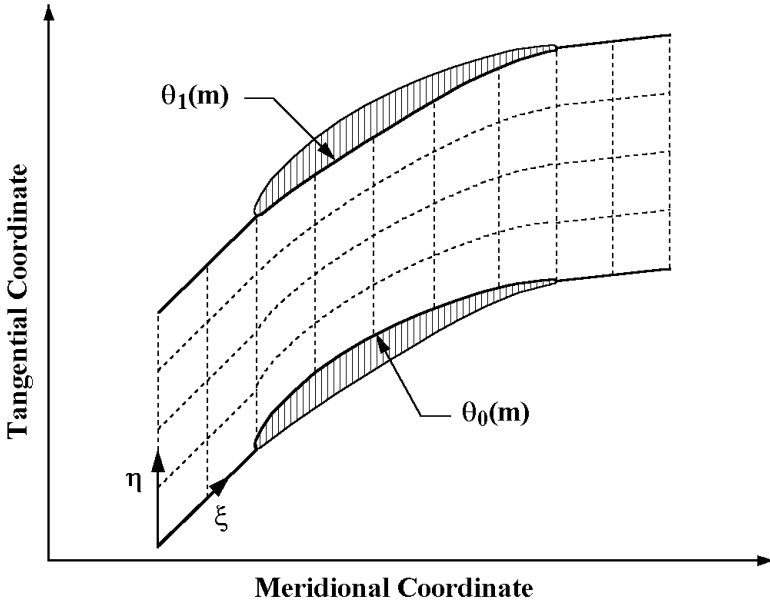


FIGURE 5-3 Blade-to-Blade Solution Domain

This transforms the complex solution domain of Fig. 5-3 into a simple rectangular domain in (ξ, η) space where η varies from 0 to 1. The blade surface tangential coordinates, θ_0 and θ_1 , are illustrated in Fig. 5-3, and β is the angle between a tangent to a constant η line and the meridional direction, i.e.,

$$\tan \beta = \left[\frac{r \partial \theta}{\partial m} \right]_{\eta} = \tan \beta_0 + [\tan \beta_1 - \tan \beta_0] \eta \quad (5-3)$$

Outside the blade passage, θ_0 and θ_1 are somewhat arbitrary, except that $\theta_1 = \theta_0 + 2\pi / N$, where N is the number of blades. Figure 5-4 shows an expanded view of a basic control volume within the solution domain from Fig. 5-3. It also illustrates special velocity components useful for developing the governing equations in (ξ, η) space. W_{ξ} and W_{η} are simply the velocity components parallel to and normal to a constant η line, respectively. The following equations relate these velocity components to the usual W_m and W_{θ} velocity components.

$$W_{\xi} = W_m \cos \beta + W_{\theta} \sin \beta \quad (5-4)$$

$$W_{\eta} = W_{\theta} \cos \beta - W_m \sin \beta \quad (5-5)$$

$$W_m = W_{\xi} \cos \beta - W_{\eta} \sin \beta \quad (5-6)$$

$$W_{\theta} = W_{\eta} \cos \beta + W_{\xi} \sin \beta \quad (5-7)$$

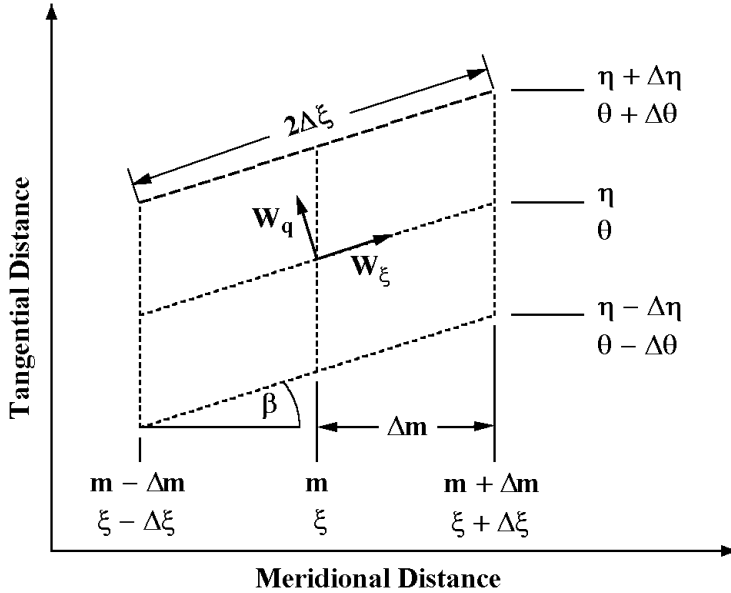


FIGURE 5-4 A Control Volume

5.3 POTENTIAL FLOW IN THE BLADE-TO-BLADE PLANE

As discussed previously, potential flow analysis on a blade-to-blade stream surface involves solution under the assumption that the absolute flow is time-steady, inviscid and adiabatic, with rothalpy and entropy both constant on this surface. No restrictions are imposed relative to variation of rothalpy and entropy normal to the stream surface. In general, rothalpy and entropy will vary from stream surface to stream surface, which is quite compatible with the present analysis. The governing equations are conservation of mass, Eq. (3-21), and the irrotationality condition, Eq. (3-29). The steady form of these equations could be transformed directly into the (ξ, η) space by developing transformations for the derivatives from Eqs. (5-1) and (5-2). But a more accurate numerical analysis is obtained by a more fundamental development using the basic control volume shown in Fig. 5-4. Conservation of mass for this control volume can be stated as

$$2\Delta m \left[\left(\frac{\rho b W_q}{\cos \beta} \right)_{m, \eta - \Delta \eta} - \left(\frac{\rho b W_q}{\cos \beta} \right)_{m, \eta + \Delta \eta} \right] + 2\Delta \eta \left[(S \rho b W_m)_{m - \Delta m, \eta} - (S \rho b W_m)_{m + \Delta m, \eta} \right] = 0 \quad (5-8)$$

where the subscripts identify specific grid points on the control volume of Fig. 5-4, and the tangential spacing, $S(m)$, is defined by

$$S = r(\theta_1 - \theta_0) \quad (5-9)$$

Taking the limit as Δm and $\Delta \eta$ approach zero, Eq. (5-8) reduces to the following continuity equation.

$$\frac{\partial}{\partial \eta} \left[\frac{\rho b W_q}{\cos \beta} \right] + \frac{\partial (S \rho b W_m)}{\partial m} = 0 \quad (5-10)$$

Developed in this fashion, it can be noted that the continuity equation contains coordinates m and η and velocity components W_q and W_m from two different coordinate systems. While perhaps a little unusual, it does result in a more precise statement of conservation of mass for use in a numerical analysis. Numerical approximations to the governing equations will apply them to a finite control volume. More accurate numerical approximations will result from using the control volume approach to develop the equations instead of using a mathematical transformation of the derivatives in Eq. (3-21). The condition for irrotational absolute flow in the stream surface requires that the component of the absolute vorticity normal to the stream sheet be zero, i.e.,

$$\vec{e}_n \cdot (\vec{\nabla} \times \vec{C}) = \vec{e}_n \cdot [\vec{\nabla} \times (\vec{W} + r\omega \vec{e}_\theta)] = 0 \quad (5-11)$$

Stokes theorem is a convenient method to impose this condition on the control volume. Stokes theorem relates the line integral of the velocity about any closed path to the integral of the normal component vorticity over the area enclosed by the path. In the rotating coordinate system, Stokes theorem can be applied as

$$\oint_C \vec{W} \cdot d\vec{r} = \int_A [\vec{e}_n \cdot (\vec{\nabla} \times \vec{W})] da = - \int_A \vec{e}_n \cdot (\vec{\nabla} \times r\omega \vec{e}_\theta) da \quad (5-12)$$

When applied to the control volume, this yields

$$\begin{aligned} & 2\Delta m \left[\left(\frac{W_\xi}{\cos \beta} \right)_{m, \eta - \Delta \eta} - \left(\frac{W_\xi}{\cos \beta} \right)_{m, \eta + \Delta \eta} \right] \\ & + 2\Delta \eta [(SW_\theta)_{m - \Delta m, \eta} - (SW_\theta)_{m + \Delta m, \eta}] = 4\Delta \eta \Delta m \frac{S}{r} \frac{\partial r^2 \omega}{\partial r} \end{aligned} \quad (5-13)$$

Taking the limit as Δm and $\Delta \eta$ approach zero, Eq. (5-13) reduces to

$$\frac{\partial}{\partial \eta} \left[\frac{W_\xi}{\cos \beta} \right] = \frac{\partial (SW_\theta)}{\partial m} + 2S\omega \sin \phi \quad (5-14)$$

where ϕ is the stream sheet angle with the axial direction as shown in Fig. 5-2. Hence,

$$\sin \phi = \frac{\partial r}{\partial m} \quad (5-15)$$

A stream function, ψ , is defined by

$$\dot{m} \frac{\partial \psi}{\partial m} = -\rho b(W_\theta - W_m \tan \beta) \quad (5-16)$$

$$\dot{m} \frac{\partial \psi}{\partial \eta} = S \rho b W_m \quad (5-17)$$

where \dot{m} is the stream sheet mass flow rate. Hence, the velocity components are given by

$$W_m = \frac{\dot{m}}{S b \rho} \frac{\partial \psi}{\partial \eta} \quad (5-18)$$

$$W_\theta = \frac{\dot{m}}{b \rho} \left[\frac{\tan \beta}{S} \frac{\partial \psi}{\partial \eta} - \frac{\partial \psi}{\partial m} \right] \quad (5-19)$$

By substituting Eqs. (5-5), (5-18) and (5-19) into Eq. (5-10), it is easily shown that the definition of ψ identically satisfies the continuity equation. Note that ψ varies from 0 to 1 as θ varies from θ_0 to θ_l or as η varies from 0 to 1. Thus, both conservation of mass and energy are satisfied, requiring solution of the irrotationality condition only to predict the inviscid flow field. Introducing the stream function into Eq. (5-14) yields the required equation.

$$\begin{aligned} & \frac{\partial}{\partial \eta} \left[\frac{\dot{m}(1 + \tan^2 \beta)}{S b \rho} \frac{\partial \psi}{\partial \eta} - \frac{\dot{m} \tan \beta}{b \rho} \frac{\partial \psi}{\partial m} \right] \\ &= \frac{\partial}{\partial m} \left[\frac{\dot{m} \tan \beta}{b \rho} \frac{\partial \psi}{\partial \eta} - \frac{\dot{m} S}{b \rho} \frac{\partial \psi}{\partial m} \right] + 2 S \omega \sin \phi \end{aligned} \quad (5-20)$$

This equation can be simplified to the form

$$A \frac{\partial^2 \psi}{\partial \eta^2} - 2B \frac{\partial^2 \psi}{\partial \eta \partial m} + C \frac{\partial^2 \psi}{\partial m^2} + D \frac{\partial \psi}{\partial \eta} + E \frac{\partial \psi}{\partial m} = 2 S \omega \sin \phi \quad (5-21)$$

where

$$A(m, \eta) = \dot{m} / (S b \rho \cos^2 \beta) \quad (5-22)$$

$$B(m, \eta) = \dot{m} \tan \beta / (b \rho) \quad (5-23)$$

$$C(m, \eta) = \dot{m} S / (b \rho) \quad (5-24)$$

$$D(m, \eta) = \frac{\partial A}{\partial \eta} - \frac{\partial B}{\partial m} \quad (5-25)$$

$$E(m, \eta) = \frac{\partial C}{\partial m} - \frac{\partial B}{\partial \eta} \quad (5-26)$$

Boundary conditions for $\psi(m, \eta)$ on the solution domain shown in Fig. 5-3 are reasonably straightforward. On the blade surfaces,

$$\psi(m, 0) = 0 \quad (5-27)$$

$$\psi(m, 1) = 1 \quad (5-28)$$

For the side boundaries outside of the blade passage, the periodicity condition is used. Since the flow is identical in all blade passages, the flow field must repeat in the tangential direction with a period of $\Delta\eta = 1$. The periodic nature of the flow can be used to extend the solution into adjacent passages such that points on these side boundaries can be treated the same as interior points in the solution domain.

$$\psi(m, \eta + 1) = \psi(m, \eta) + 1 \quad (5-29)$$

$$\rho(m, \eta + 1) = \rho(m, \eta) \quad (5-30)$$

$$W_m(m, \eta + 1) = W_m(m, \eta) \quad (5-31)$$

$$W_\theta(m, \eta + 1) = W_\theta(m, \eta) \quad (5-32)$$

Conditions on the upstream and downstream boundaries may be assigned as uniform flow, basically requiring that ψ vary linearly in the tangential direction. But reliability of the numerical analysis is improved if a less stringent boundary condition is imposed. A good choice is to require that the flow angle be constant on these boundaries. Then, if the geometry of the side boundaries is defined such that β equals the local flow angle on the upstream and downstream boundaries, the appropriate upstream and downstream boundary condition is

$$\frac{\partial \psi}{\partial \xi} = \cos \beta \frac{\partial \psi}{\partial m} = 0 \quad (5-33)$$

as can be seen from Eq. (5-16). Typically, β will be assigned to vary uniformly along the side boundary from the upstream boundary flow angle to the blade leading edge blade angle, and analogously for the downstream boundary. Once this distribution of β along the side boundaries is specified, simple integration of Eq. (5-3) yields $\theta_0(m)$ and $\theta_I(m)$, noting that $\beta_0 = \beta_I$ outside the blade passage. A potential flow analysis can be accomplished for virtually any specified flow angles at the upstream and downstream boundary. But, in reality, these two flow angles are not independent. A prediction of the downstream flow angle for any

upstream flow conditions is to be preferred. To accomplish this, some additional constraint is required. Typically, the well-known Kutta condition is applied at the trailing edge. This simply requires that the pressures on the two sides of the blades must be equal at the trailing edge. This follows from the fact that there is no longer a tangential blade force to sustain a pressure difference. It is equivalent to imposing the following trailing edge condition.

$$[W(m,0)]_{te} = [W(m,1)]_{te} \quad (5-34)$$

Typically, iterative adjustment of the discharge flow angle is accomplished as part of the solution process until a value that satisfies Eq. (5-34) is found.

Equation (5-21) is solved subject to the above boundary conditions while treating the gas density field throughout the solution domain as constant, starting with an initial guess for the density field. After the stream function is predicted, Eqs. (5-18) and (5-19) are used to compute the velocity field. Then, the density field is updated using an appropriate equation of state from Chapter 2. The stream function is then recalculated, and the process continued until convergence is achieved. A grid structure is developed over the solution domain, as illustrated in Fig. 5-3. The spacing between nodes Δm and $\Delta \eta$ is constant in each direction. Unequal spacing can be used, but this writer's experience has shown that the benefits of unequal spacing do not justify the added complexity and reduced computational speed. Equation (5-21) is reduced to linear form using standard finite-difference approximations for the derivatives. If subscripts i and j are used to designate the i th meridional node and the j th tangential node, the relevant finite-difference approximations for interior points are

$$\frac{\partial \psi}{\partial m} = \frac{\psi_{i+1,j} - \psi_{i-1,j}}{2\Delta m} \quad (5-35)$$

$$\frac{\partial \psi}{\partial \eta} = \frac{\psi_{i,j+1} - \psi_{i,j-1}}{2\Delta \eta} \quad (5-36)$$

$$\frac{\partial^2 \psi}{\partial m^2} = \frac{\psi_{i+1,j} - 2\psi_{i,j} + \psi_{i-1,j}}{(\Delta m)^2} \quad (5-37)$$

$$\frac{\partial^2 \psi}{\partial \eta^2} = \frac{\psi_{i,j+1} - 2\psi_{i,j} + \psi_{i,j-1}}{(\Delta \eta)^2} \quad (5-38)$$

$$\frac{\partial^2 \psi}{\partial m \partial \eta} = \frac{\psi_{i+1,j+1} - \psi_{i-1,j+1} - \psi_{i+1,j-1} + \psi_{i-1,j-1}}{4\Delta m \Delta \eta} \quad (5-39)$$

Equations (5-35) through (5-39) are easily derived using truncated Taylor series expansions of ψ as functions of m and η (Aungier, 2000). The terms D and E in Eqs. (5-25) and (5-26) require approximations for the first derivatives at nodes on the boundary. These can be developed in the same way as for interior points. They are

$$\frac{\partial \psi}{\partial m} = \frac{4\psi_{i+1,j} - 3\psi_{i,j} - \psi_{i+2,j}}{2\Delta m} \quad (5-40)$$

$$\frac{\partial \psi}{\partial \eta} = \frac{4\psi_{i,j+1} - 3\psi_{i,j} - \psi_{i,j+2}}{2\Delta \eta} \quad (5-41)$$

$$\frac{\partial \psi}{\partial m} = \frac{3\psi_{i,j} - 4\psi_{i-1,j} + \psi_{i-2,j}}{2\Delta m} \quad (5-42)$$

$$\frac{\partial \psi}{\partial \eta} = \frac{3\psi_{i,j} - 4\psi_{i,j-1} + \psi_{i,j-2}}{2\Delta \eta} \quad (5-43)$$

Substitution of the finite-difference approximations into Eq. (5-21) for any interior node (i, j) yields a simple linear equation for ψ

$$\begin{aligned} \psi_{i,j} + \tilde{A}_{i,j}\psi_{i-1,j} + \tilde{B}_{i,j}\psi_{i+1,j} + \tilde{C}_{i,j}\psi_{i,j-1} + \tilde{D}_{i,j}\psi_{i,j+1} \\ + \tilde{E}_{i,j}[\psi_{i+1,j+1} - \psi_{i+1,j-1} - \psi_{i-1,j+1} + \psi_{i-1,j-1}] = \tilde{Q}_{i,j} \end{aligned} \quad (5-44)$$

The coefficients in Eq. (5-44) are given by

$$\tilde{A}_{i,j} = - \left[\frac{C_{i,j}}{(\Delta m)^2} - \frac{E_{i,j}}{2\Delta m} \right] / \left[\frac{2A_{i,j}}{(\Delta \eta)^2} + \frac{2C_{i,j}}{(\Delta m)^2} \right] \quad (5-45)$$

$$\tilde{B}_{i,j} = - \left[\frac{C_{i,j}}{(\Delta m)^2} + \frac{E_{i,j}}{2\Delta m} \right] / \left[\frac{2A_{i,j}}{(\Delta \eta)^2} + \frac{2C_{i,j}}{(\Delta m)^2} \right] \quad (5-46)$$

$$\tilde{C}_{i,j} = - \left[\frac{A_{i,j}}{(\Delta \eta)^2} - \frac{D_{i,j}}{2\Delta \eta} \right] / \left[\frac{2A_{i,j}}{(\Delta \eta)^2} + \frac{2C_{i,j}}{(\Delta m)^2} \right] \quad (5-47)$$

$$\tilde{D}_{i,j} = - \left[\frac{A_{i,j}}{(\Delta \eta)^2} + \frac{D_{i,j}}{2\Delta \eta} \right] / \left[\frac{2A_{i,j}}{(\Delta \eta)^2} + \frac{2C_{i,j}}{(\Delta m)^2} \right] \quad (5-48)$$

$$\tilde{E}_{i,j} = \left[\frac{B_{i,j}}{2\Delta m \Delta \eta} \right] / \left[\frac{2A_{i,j}}{(\Delta \eta)^2} + \frac{2C_{i,j}}{(\Delta m)^2} \right] \quad (5-49)$$

$$\tilde{Q}_{i,j} = - [2S\omega \sin \phi] / \left[\frac{2A_{i,j}}{(\Delta \eta)^2} + \frac{2C_{i,j}}{(\Delta m)^2} \right] \quad (5-50)$$

Numerical solution of the linearized stream function equation can be accomplished with a relaxation technique (Katsanis 1968, 1969) or a matrix method (Smith and Frost, 1969; Aungier, 2000). This writer has used both methods and has found the matrix method to be superior in both computational speed and reliability. In the matrix method, Eq. (5-44) is used to develop equations for all nodes, resulting in a matrix equation, where the major matrix is a square matrix with the number of rows and columns equal to the number of nodes. It is a very sparse matrix, having non-zero values only in a band about its diagonal, so that a

rather small number of values actually need to be stored in the computer's memory. Aungier (2000) provides a rather detailed description of a very efficient matrix solution for this problem.

After each solution for the stream function, the density field must be updated using a new velocity field estimate from Eqs. (5-18) and (5-19). Since rothalpy is constant on the stream sheet, Eqs. (3-11) and (3-13) require

$$h = H' - \frac{1}{2} W^2 = I + \frac{1}{2} (r\omega)^2 - \frac{1}{2} W^2 \quad (5-51)$$

And, since entropy is also constant on the stream sheet, all thermodynamic properties can be calculated as a function of (h, s) , using an appropriate equation of state from Chapter 2. While conducting iterations to converge on a density field, convergence on a discharge flow angle to satisfy the Kutta condition, Eq. (5-34), is also accomplished. As long as the flow is subsonic, this procedure of lagging the density solution one iteration behind the stream function solution offers excellent numerical stability and rapid convergence. Once velocities greater than sonic velocity are encountered, the solution will become unstable, and will almost always diverge. Blade-to-blade flow problems involving local patches of supersonic flow are often encountered in axial-flow compressor analysis. The usefulness of a potential flow analysis is greatly increased if it is extended to be capable of addressing these transonic flow cases. This can be accomplished by readjusting the mass flow rate and speed, or the inlet total sound speed, such that the inlet velocity triangle is the same as the actual problem but all velocities are subsonic. After solving the subsonic flow problem, the streamline pattern is assumed to be correct, and some type of streamline curvature numerical technique can be used to calculate the flow for the actual inlet conditions. Katsanis (1969) is a good example of this type of extension of a potential flow solution. The weakness in this approach is that the resulting flow field will no longer satisfy the irrotationality condition. Aungier (2000) presents a better technique, which can predict an irrotational flow field that conserves mass and involves local patches of supersonic flow. The inlet total sound speed is adjusted to reduce all velocities to subsonic values. At the same time, the stream sheet thickness distribution is adjusted such that the resident velocity field, which conserves mass for the fictitious subsonic problem, will also conserve mass for the actual transonic flow problem when the actual inlet conditions and steam sheet thickness distribution are used. Thus, when the subsonic flow solution is obtained, it is only necessary to accomplish a final update of all thermodynamic data with the predicted velocity field to satisfy all governing equations for the transonic flow case. Implementation of this extension to the analysis is straightforward, but depends to some degree on the equation of state used in the analysis. Aungier (2000) provides an illustration of its implementation for the special case of a calorically and thermally perfect gas.

The stability of a numerical solution of the blade-to-blade flow problem can be significantly influenced by the manner in which the grid structure is established near the leading and trailing edges of the blades. Figure 5-5 illustrates two methods of locating the grid near the leading edge. In one case, the first nodes on the blade surface are outside the passage, touching the blade at a single point. The other case locates the first nodes on the blade surfaces inside the passage with a

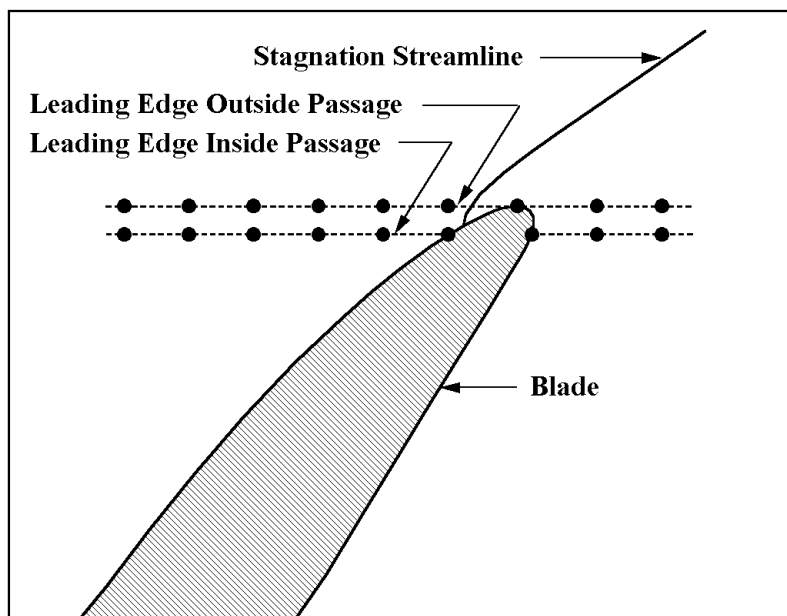


FIGURE 5-5 Leading Edge Grid Structure

node on each blade surface. Experience has shown that the first method can result in local numerical instability, while the second method almost never experiences that problem. The cause of instability has been traced to the behavior of the stagnation streamline, coupled with the finite-difference approximations for derivatives with respect to η used at blade surface points. In the illustration in Fig. 5-5, it is seen that the stagnation streamline passes between the blade surface and the node next to the surface when the leading edge nodes are outside the passage. Since ψ has the same value on the stagnation streamline and the blade surface, a difference approximation to the tangential derivative will provide a poor estimate. And, without special logic in the solution, it is not obvious which direction the tangential difference approximation for the node on the blade should use, i.e., Eq. (5-41) or (5-43). In the case illustrated, nodes to the right of the leading edge node should be used, i.e., Eq. (5-41). Minor changes in gas density at the leading edge can induce the stagnation streamline to move, possibly even making it shift to the opposite blade surface. It is not uncommon for this to result in an oscillation on successive iterations, all occurring very local to this region, such that a converged solution is never realized. Numerical damping, refining the grid near the leading edge, etc., can alleviate this problem. But a simpler and more effective approach is to move the leading edge nodes into the passage as illustrated in Fig. 5-5. This removes the ambiguity regarding the direction to be used for the surface derivatives, and the local oscillation problem almost never occurs when this is done. It is a very simple method to avoid the tendency toward local instability near the leading and trailing edges.

Figure 5-6 illustrates typical results from this potential flow solution. Predicted blade surface Mach numbers are compared to experimental results reported by Dunavant et al. (1955). For the purpose of a blade loading diagram comparison, the experimental surface pressure coefficient data were converted to Mach numbers using standard compressible flow relations. This is really the same example used in Aungier (2000), but the analysis is now capable of a more precise treatment of the blade geometry. Basically, the methods described in Chapter 4 are now included in the analysis to very precisely define the blade geometry for standard axial-flow compressor blade camberlines and profiles. Overall, rather good agreement is achieved between predictions and experiment. Near the trailing edge, the boundary layer analysis described later in this chapter predicts boundary layer separation as noted in Fig. 5-6. This would be expected to suppress further diffusion of the velocity, much as seems to have occurred in the experiment. Some additional insight into the quality of the predicted results is provided from empirical blade performance correlations that are described in the next chapter. For this particular cascade test, those correlations indicate that the angle of attack is within 0.5° of the optimum value. Noting that the predicted Mach numbers on the two sides of the blade are nearly equal at the leading edge, the analysis indicates that the flow enters the blade smoothly, which is often used as an indication of an optimum inlet angle. Indeed, these predicted Mach numbers should not be expected to be exactly equal under optimum inlet conditions, since the leading edge node structure lies inside the passage as described previously. In effect, the leading edge predicted values are slightly downstream of the true entrance point for the flow. The potential flow analysis predicts a discharge

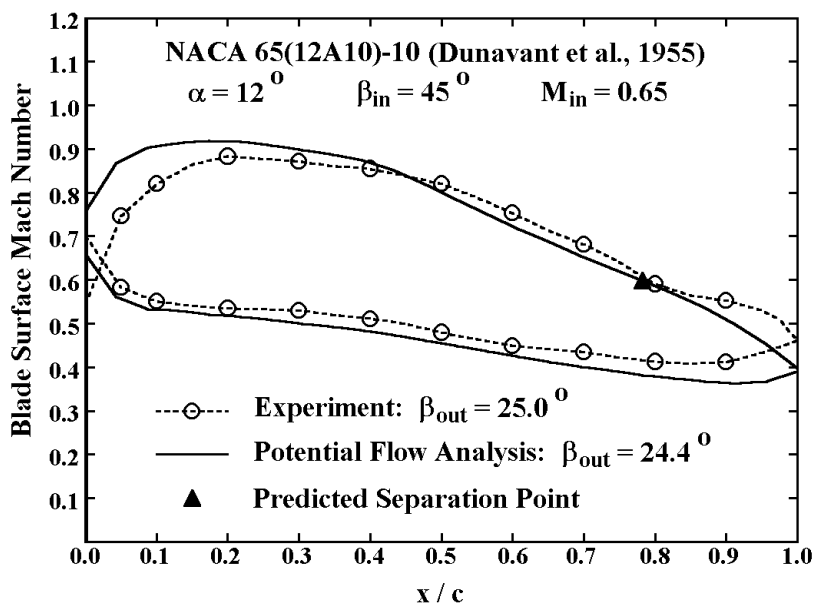


FIGURE 5-6 Potential Flow Results

flow angle of 24.4° , which is in reasonably good agreement with the experimental value of 25.0° . Hence, this potential flow analysis provides very useful information about the performance of this cascade that is consistent with the cascade test results and with empirical cascade performance models from Chapter 6.

Figure 5-7 illustrates the transonic capability of this extended potential flow analysis. The case shown is the same as that used for Fig. 5-6, except that the higher inlet Mach number results in a substantial supersonic patch within the flow field. The agreement between the predictions and the experimental data of Dunavant et al. (1955) is reasonably good, both in terms of the blade loading diagram and the discharge flow angle. The procedure used is very robust, providing rapid and reliable convergence on these transonic flow problems. It is a very valuable extension for axial-flow compressor analysis, permitting much wider use of the potential flow method and resulting in far fewer solution failures. As long as Mach numbers do not become so large that imbedded shock waves significantly influence the flow, the predictions are generally quite accurate as well, as evidenced by this comparison with experimental data.

5.4 LINEARIZED POTENTIAL FLOW ANALYSIS

The two-dimensional potential flow analysis of the previous section can be simplified to provide an exceptionally fast blade-to-blade flow analysis, yet provide surprisingly good prediction accuracy [Aungier, 1988(a), 2000]. If the sole

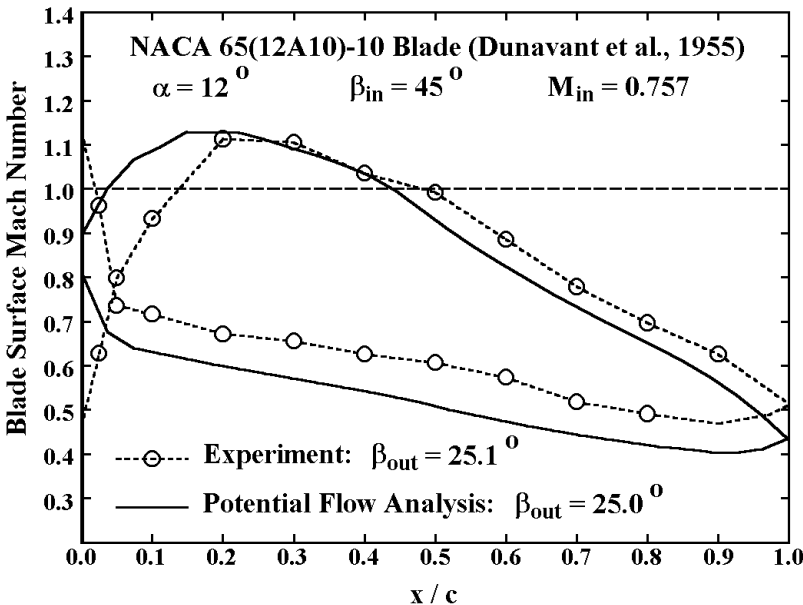


FIGURE 5-7 Transonic Potential Flow Solution

purpose of an analysis is to accomplish stand-alone blade-to-blade flow prediction, there is really little reason to consider this simplified model. The two-dimensional potential flow analysis described above is so fast that it is not necessary to accept any compromise in accuracy for increased computation speed. The real purpose of the linearized method is its use in a quasi-three-dimensional flow analysis, where blade-to-blade analyses are conducted on several stream sheets and must be repeated many times. It is described here to prepare for its later use in that more general application.

The linearized blade-to-blade model is nothing more than a simplification of the potential flow model of the previous section. The stream function is approximated by

$$\psi(m, \eta) = a(m)[\eta - \eta^2] + \eta^2 \quad (5-52)$$

From Eq. (5-17) it is easily shown that this is equivalent to assuming that the quantity $\rho b W_m$ varies linearly with η . Equation (5-14) will be solved in integral form, noting that $W = W_\xi$ on the blade surfaces, i.e.,

$$\frac{W_1}{\cos \beta_1} - \frac{W_0}{\cos \beta_0} = \int_0^1 \frac{\partial SW_\theta}{\partial m} d\eta + 2S\omega \sin \phi \quad (5-53)$$

The velocity normal to the blade surfaces must be zero, which requires that

$$W = \frac{W_m}{\cos \beta} = \frac{1}{\cos \beta} \frac{\dot{m}}{Sb\rho} \frac{\partial \psi}{\partial \eta} \quad (5-54)$$

Combining Eqs. (5-52), (5-53) and (5-54) yields

$$\frac{W_1}{\cos \beta_1} = \frac{\dot{m}(2-a)}{Sb\rho \cos^2 \beta_1} \quad (5-55)$$

$$\frac{W_0}{\cos \beta_0} = \frac{\dot{m}a}{Sb\rho \cos^2 \beta_0} \quad (5-56)$$

which supply the terms on the left-hand side of Eq. (5-53). From Eqs. (5-18), (5-19) and (5-52)

$$SW_\theta = \dot{m}[\tan \beta(a - 2a\eta + 2\eta) - a'S(\eta - \eta^2)] / (b\rho) \quad (5-57)$$

where the prime notation denotes the total derivative with respect to m . As was done with the two-dimensional potential flow analysis, the stream function solution will be accomplished with the density held constant. To simplify the equations to follow, define

$$u(m, \eta) = \dot{m} \tan \beta / (b\rho) \quad (5-58)$$

$$v(m, \eta) = \dot{m} S / (b\rho) \quad (5-59)$$

Differentiating Eq. (5-57) and introducing Eqs. (5-58) and (5-59) yields

$$\frac{\partial SW_\theta}{\partial m} = \frac{\partial u}{\partial m} (a - 2a\eta + 2\eta) + (1 - 2\eta)ua' - (va'' + \frac{\partial v}{\partial m} a')(\eta - \eta^2) \quad (5-60)$$

Using truncated Taylor series expansions for any function, $F(\eta)$, for values at $\eta = 0, 0.5$ and 1 , a three-point difference approximation to the integral is obtained.

$$\int_0^1 F(\eta) d\eta = (F_0 + 4\bar{F} + F_1) / 6 \quad (5-61)$$

where the overbar designates a value at $\eta = 0.5$. With the above equations and some tedious algebra, the integral term in Eq. (5-53) is given by

$$\int_0^1 \frac{\partial SW_\theta}{\partial m} d\eta = [au'_0 + u_0a' + 4\bar{u}' - \bar{v}a'' - \bar{v}'a' + u'_1(2 - a) - u_1a'] / 6 \quad (5-62)$$

Combining Eqs. (5-53), (5-55), (5-56) and (5-62) yields a simple linear differential equation.

$$a'' + Aa' + Ba = C \quad (5-63)$$

where A, B and C are functions of m only

$$A(m) = [\bar{v}' - u_0 + u_1] / \bar{v} \quad (5-64)$$

$$B(m) = \frac{u'_1 - u'_0}{\bar{v}} - \frac{6}{\bar{v}S^2} \left[\frac{v_1}{\cos^2 \beta_1} + \frac{v_0}{\cos^2 \beta_0} \right] \quad (5-65)$$

$$C(m) = \frac{2u'_1 + 4\bar{u}' + 12\omega \sin \phi}{\bar{v}} - \frac{12v_1}{\bar{v}S^2 \cos^2 \beta_1} \quad (5-66)$$

Equation (5-63) is solved from the blade leading edge to the trailing edge. The leading edge boundary condition follows from the known inlet angular momentum supplied by the upstream flow, $W_{\theta, in}$. Integrating W_θ across the passage at the leading edge using Eq. (5-61) yields the following leading edge boundary condition.

$$a' + a[u_1 - u_0] / \bar{v} = [4\bar{u} + 2u_1 - 6SW_{\theta, in}] / \bar{v} \quad (5-67)$$

The Kutta condition is again used as the trailing edge boundary condition, i.e., $W_0 = W_l$ at the trailing edge. From Eqs. (5-55) and (5-56), the trailing edge boundary condition is

$$a = 2 \cos \beta_0 / [\cos \beta_1 + \cos \beta_0] \tag{5-68}$$

The governing equation is cast in finite-difference form using the difference approximations previously introduced to develop a matrix equation for solution. In this case, a simple tri-diagonal matrix is obtained, except for the equation at the leading edge point, which contains one extra term. Inversion of this matrix is a rather trivial problem for the numerical analysis, which results in an exceptionally efficient blade-to-blade flow analysis. The iteration process to update the gas density field follows the same process as that for the two-dimensional potential flow, and the same transonic flow extension is incorporated. Aungier (2000) provides a fairly detailed description of the numerical analysis used to implement this model.

Figure 5-8 compares results from the linearized and two-dimensional potential flow analyses for the same test case used earlier. The linearized method does not resolve the blade loading too well near the leading edge, but does reasonably well over most of the blade. The linearized method predicts a discharge flow angle for this case of 25.8°, which is in reasonably good agreement with the experimental value of 25.0°. The blade surface flow predictions at the leading edge are generally ignored, since the solution imposes the upstream boundary condition at that point. It will, by definition, correctly match the average angular momentum at the leading edge, but not necessarily the blade surface data, particularly on relatively blunt blades such as this one. Later in this book, it will be seen that the role of this

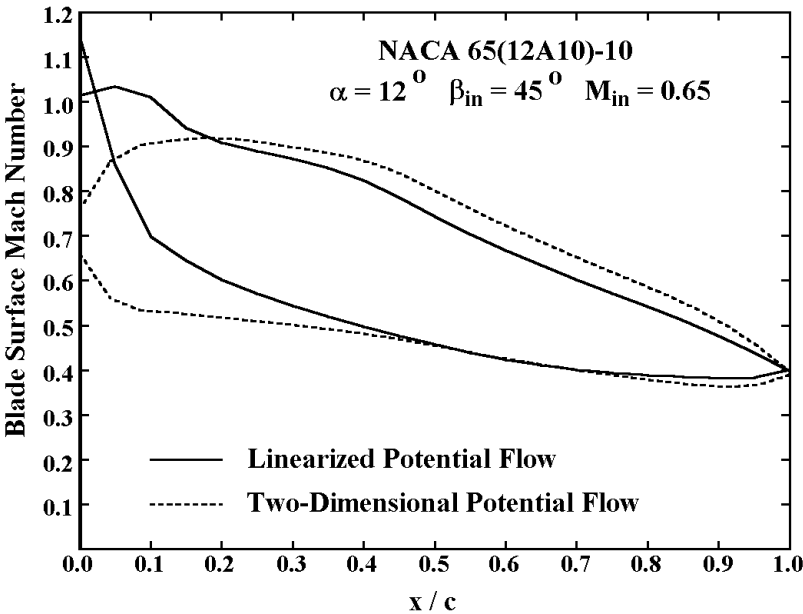


FIGURE 5-8 Linearized Potential Flow Results

analysis in a quasi-three-dimensional flow analysis is to define the streamwise variation of the average angular momentum, which it does rather well. Typical practice is to provide a direct and automated interface to the two-dimensional method for a detailed blade loading analysis after the quasi-three-dimensional flow analysis is completed. At that point, the stream sheet geometry and flow conditions are well defined for input to the two-dimensional method. The advantage offered by the linearized method for the quasi-three-dimensional flow application is exceptional computation speed while accurately estimating the average angular momentum distribution through the blade passage.

5.5 THE TIME-MARCHING METHOD

The potential flow method can be applied to a very wide range of axial-flow compressor blade-to-blade flow problems, particularly with the transonic flow extension. But when Mach numbers become too high, a more general analysis technique is needed. The time-marching method provides a more general solution capability that is suitable for subsonic, supersonic or mixed subsonic-supersonic flow problems. Von Neumann and Richtmyer (1950) suggested this method for treating flows with imbedded shock waves. Except for some interest from mathematicians (Lax, 1954; Lax and Wendroff, 1964), the method received little attention until computers evolved enough for it to be used on practical problems. This writer participated in the development of this technique for application to hypersonic reentry vehicles in the late 1960s [Aungier, 1968, 1970, 1971(a), 1971(b)]. Soon after its successful application to the reentry problem, the method became popular for the blade-to-blade flow problem (e.g., Gopolkrishnan and Bozzola, 1973; Denton, 1982). The time-marching technique of Aungier [1970, 1971(a), 1971(b)] has also been adapted to this application and later reported in Aungier (2000). An abbreviated description of this technique that is sufficient to understand the fluid dynamics of the problem is provided in this chapter. Readers interested in developing a numerical analysis to implement the procedure may find the expanded description in Aungier (2000) helpful.

The time-marching solution will be accomplished using the same solution domain, velocity components and coordinate system as those used for the potential flow analysis, i.e., Fig. 5-3 and Eqs. (5-1) through (5-7). The governing equations are Eqs. (3-21), (3-22), (3-23) and (3-25), which are to be solved over the stream sheet in their full time-unsteady form. The solution is advanced in time until the flow becomes approximately steady with time. The solution approaches the steady state asymptotically, so a true steady-state solution is never actually achieved. Rather, the solution is advanced in time until variations with time are considered negligible. As was discussed previously for the potential flow analysis, it is not advisable to simply transform the derivatives in the governing equations to solve them in the (ξ, η) coordinate system. A more precise numerical analysis will be achieved by developing the equations for the control volume to be used in the solution. This is accomplished by applying the integral form of the equations of motion to the control volume in Fig. 5-4. The integral form of the continuity, momentum and energy equations for inviscid, time-unsteady flow are

$$\int_V \frac{\partial \rho}{\partial t} dV + \int_A \rho (\vec{W} \cdot \vec{n}) dA = 0 \quad (5-69)$$

$$\int_V \frac{\partial \rho}{\partial t} \vec{W} dV + \int_A \rho \vec{W} (\vec{W} \cdot \vec{n}) dA + \int_A P \vec{e} (\vec{e} \cdot \vec{n}) dA = \int_V \vec{f} dV \quad (5-70)$$

$$\int_V \left[\rho \frac{\partial H'}{\partial t} - \frac{\partial P}{\partial t} \right] dV + \int_A \rho H' (\vec{W} \cdot \vec{n}) dA = \int_V \rho (\vec{f} \cdot \vec{W}) dV \quad (5-71)$$

where V and A denote volume and area integrals, respectively, \vec{n} is a unit vector normal to the area and directed out of the control volume, \vec{e} is a unit vector along \vec{w} and \vec{f} is a body force. The body force is used to account for the Coriolis and centrifugal acceleration terms in the rotating curvilinear coordinate system. After some tedious algebra, application of these integral equations to the control volume yield:

$$Sb \frac{\partial \rho}{\partial t} + \frac{\partial}{\partial m} [Sb \rho W_m] + \frac{\partial}{\partial \eta} [b \rho Q] = 0 \quad (5-72)$$

$$\begin{aligned} Sb \frac{\partial \rho W_m}{\partial t} + \frac{\partial}{\partial m} [Sb(\rho W_m^2 + P)] - \tan \beta \frac{\partial b P}{\partial \eta} + \frac{\partial}{\partial \eta} [b \rho Q W_m] \\ = \frac{1}{r} S B \rho \sin \phi (W_\theta + r\omega)^2 + P \frac{\partial Sb}{\partial m} \end{aligned} \quad (5-73)$$

$$Sb \frac{\partial \rho W_\theta}{\partial t} + \frac{1}{r} \frac{\partial}{\partial m} [r Sb \rho W_m (W_\theta + r\omega)] + \frac{\partial}{\partial \eta} [b(\rho Q W_\theta + P)] = r\omega \frac{\partial}{\partial m} [Sb \rho W_m] \quad (5-74)$$

$$Sb \frac{\partial (\rho I - P)}{\partial t} + \frac{\partial}{\partial m} [Sb \rho W_m I] + \frac{\partial}{\partial \eta} [b \rho Q I] = 0 \quad (5-75)$$

These equations have been written in conservation form, such that they will be valid when applied across a shock wave as suggested by Lax (1954). Since shock waves can form when the flow is supersonic, this is an important consideration in the time-marching method. The parameter Q is a special velocity component to conserve properties at the constant η boundaries of the control cell, defined by

$$Q = W_q / \cos \beta = W_\theta - W_m \tan \beta \quad (5-76)$$

Note that $Q = W_q = 0$ for points on the blade surface. For these points, there is only one velocity component, W_ξ . Applying the integral momentum equation in the ξ direction yields a special momentum equation for points on the blade surfaces.

$$\begin{aligned} Sb \frac{\partial \rho W_\xi}{\partial t} + \frac{\partial}{\partial m} [Sb(\rho W_m W_\xi + P \cos \beta)] + \frac{\partial}{\partial \eta} [b \rho Q W_\xi] \\ = P \frac{\partial}{\partial m} [Sb \cos \beta] + Sb \rho \sin \phi \cos \beta r \omega^2 \end{aligned} \quad (5-77)$$

$$W_m = W_\xi \cos \beta \quad (5-78)$$

$$W_\theta = W_\xi \sin \beta \quad (5-79)$$

Equations (5-77) through (5-79) replace Eqs. (5-73) and (5-74) for points on the blade surfaces.

The boundary condition for blade surface points is that the velocity normal to the surface is zero, which is satisfied by Eqs. (5-78) and (5-79). For the side boundaries outside of the blade passage, the procedure used is the same as that for the potential flow problem, i.e., the solution is extended into adjacent passages using the periodicity condition so these points can be treated in the same fashion as any interior point. The upstream and downstream boundaries require more care. The number and type of boundary conditions depend on how these boundaries are influenced by the flow inside the solution domain. A fundamental property of hyperbolic differential equations is that there are certain characteristic directions along which derivatives of the dependent variables normal to these “characteristics” can be discontinuous. For each characteristic direction, certain dependent variables can be determined by integration along them. Aungier (2000) derives the characteristic directions for the unsteady flow problem for the upstream and downstream boundaries. Since W_m is normal to these boundaries, these unsteady characteristics are defined by

$$\frac{dm}{dt} = W_m + a \quad (5-80)$$

$$\frac{dm}{dt} = W_m - a \quad (5-81)$$

$$\frac{dm}{dt} = W_m \quad (5-82)$$

This simply shows that information can be transmitted within the flow field by waves traveling at the fluid velocity and waves where the fluid velocity is augmented or opposed by the local acoustic velocity. Aungier (2000) also shows that the characteristics of Eqs. (5-80) and (5-81) determine W_m and P , while the characteristic of Eq. (5-82) determines W_θ and I . These characteristics can be used to define the number and type of boundary conditions needed for the upstream and downstream boundaries. Figure 5-9 shows these three characteristics drawn on an m - t diagram for an upstream boundary with a subsonic meridional velocity component. Since one of the characteristics that determines the flow at time $t + \Delta t$ lies within the solution domain, one dependent variable on the boundary can be computed as part of the solution, while the other three must be assigned as boundary conditions. The characteristic for W_θ and I lies outside the solution domain, so both must be assigned as boundary conditions, with one more boundary condition to be supplied. A logical choice for the computed dependent variable is density. Then, P and W_m follow directly from the equation of state and the definition of rothalpy if entropy is known. The most logical upstream boundary conditions for this case are W_θ , P_t , and T_t . They are usually known conditions for

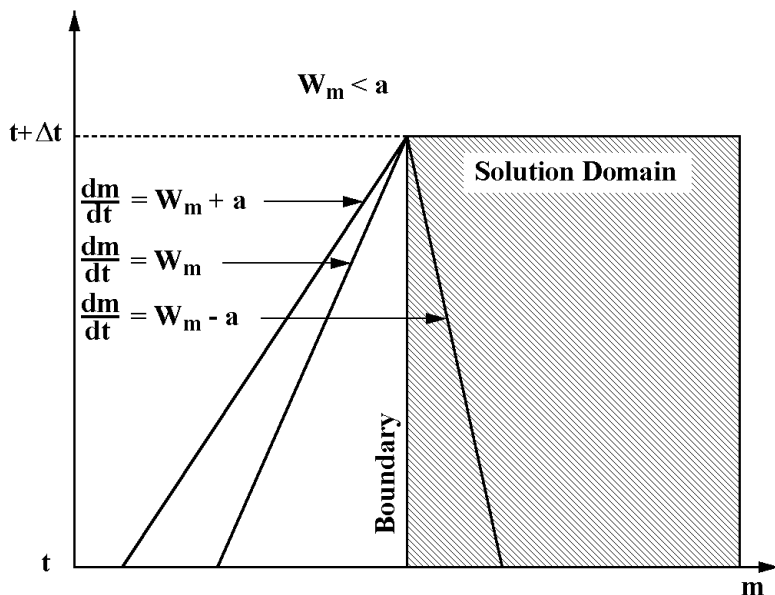


FIGURE 5-9 Subsonic Upstream Boundary

a blade-to-blade flow analysis and they specify rothalpy and entropy through the equation of state and Eq. (3-10). So, for an upstream boundary with $W_m < a$, the continuity equation will be solved for density, with all other dependent variables computed from the boundary conditions. Figure 5-10 shows the m - t diagram for an upstream boundary where the meridional velocity component is supersonic. Here, all of the characteristics that determine the flow at $t + \Delta t$ lie outside of the solution domain. Consequently, none of the dependent variables on this boundary can be computed from the solution. All dependent variables must be assigned as boundary conditions when $W_m > a$ on an upstream boundary. Figure 5-11 shows the m - t diagram for a downstream boundary where the meridional velocity component is subsonic. Here, one of the characteristics that determine the flow at $t + \Delta t$ lies outside the solution domain. This means that one dependent variable must be specified as a boundary condition, while the other three are computed as part of the solution. The usual practice is to specify the discharge static pressure as the boundary condition. It can be convenient to specify the mass flow rate instead, but then the solution procedure must compute the discharge pressure needed to produce that mass flow rate. Figure 5-12 shows the m - t diagram for a downstream boundary where the meridional velocity component is supersonic. Here, all of the characteristics that determine the flow at $t + \Delta t$ lie inside the solution domain. This means that all dependent variables can be computed from the solution, with no boundary conditions required. Usually, it is not possible to state that W_m is supersonic. That is a very unique case for each set of

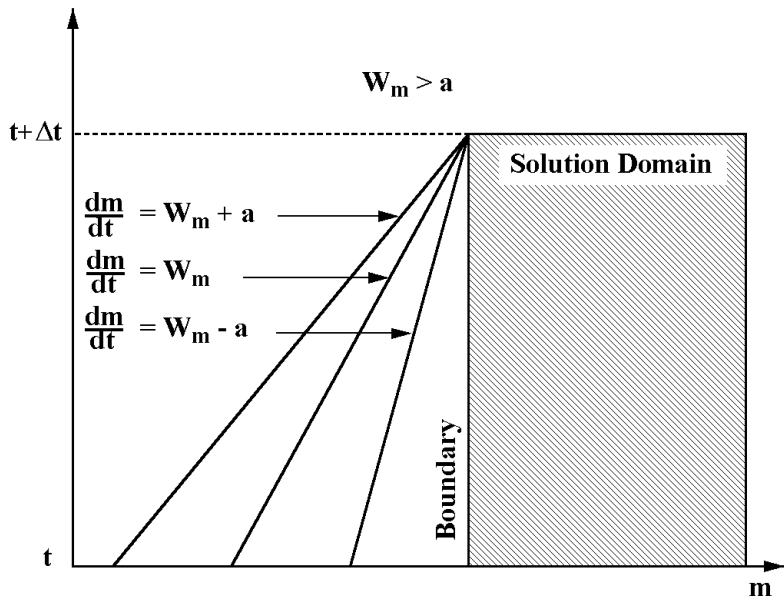


FIGURE 5-10 Supersonic Upstream Boundary

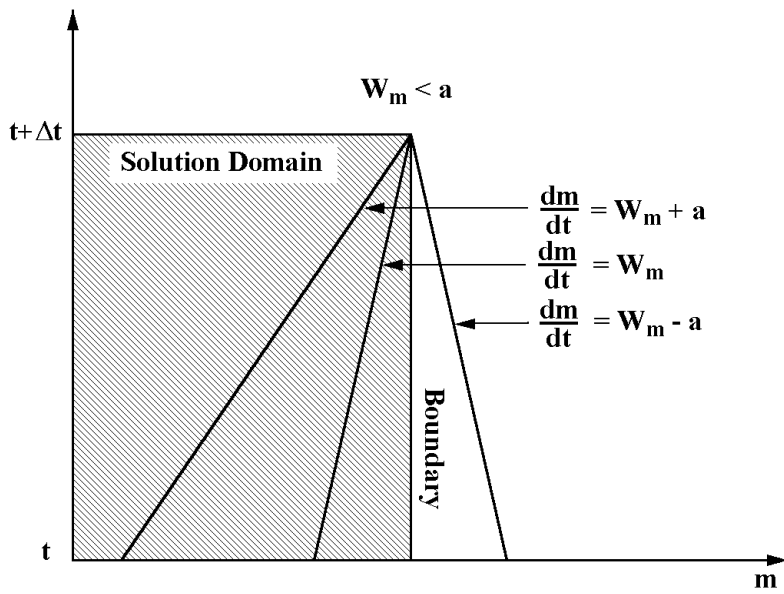


FIGURE 5-11 Subsonic Downstream Boundary

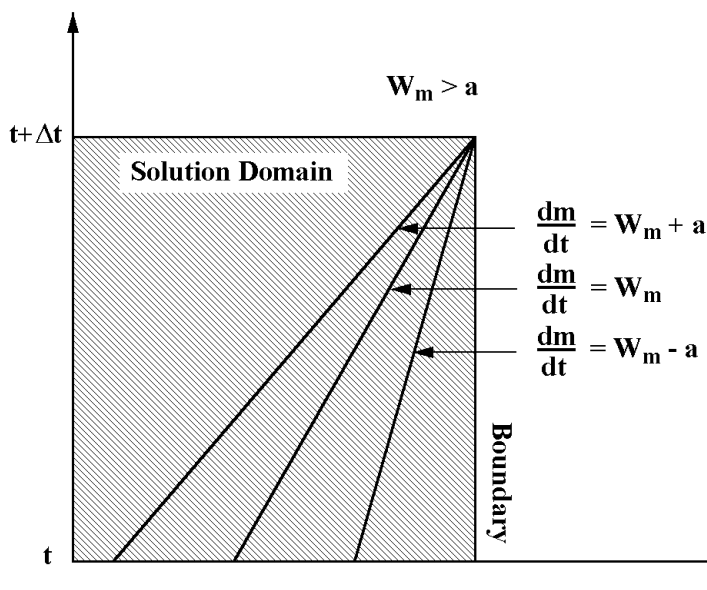


FIGURE 5-12 Supersonic Downstream Boundary

specified upstream boundary conditions. Rather, the discharge static pressure is normally specified in all cases. If the solution requires $W_m > a$ to achieve that pressure, the solution procedure must ignore the boundary condition and compute all discharge conditions. In contrast to the potential flow analysis, it is noted that no empirical Kutta condition has been needed. Indeed, there would be no way to actually use it, since W_θ is always computed at the downstream boundary as part of the solution. If W_θ were specified as a boundary condition, a Kutta condition would be needed to select a value. Indirectly, the Kutta condition is applied by virtue of the periodicity condition for all solution points downstream of the trailing edge. It is important to note that the boundary condition requirements are not optional. For example, specifying more boundary conditions than outlined here will not produce a valid solution, and normally will cause the solution to diverge. Some investigators use the unsteady characteristics directly to solve for independent variables on the boundaries, e.g., Gopalakrishnan and Bozzola (1973). In most cases this just complicates the analysis for no good reason. The same thing is accomplished by simple upstream or downstream differences in the governing equations using Eqs. (5-40) and (5-42) with far less numerical logic. On occasion, unsteady characteristics can be used to advantage at boundary points. For example, this writer used them for the upstream bow shock boundary in the hypersonic reentry problem [Aungier, 1970, 1971(a), 1971(b)]. But there really is no merit to using them in the present application. The important role of unsteady characteristics is to identify the type of and the number of boundary conditions required.

A major issue to be addressed in a time-marching solution is numerical stability. It is well known that a finite-difference solution of the governing equations that is explicit in time is unconditionally unstable. The term explicit in time refers to predicting flow data at time $t + \Delta t$ from conditions at time t . In contrast, implicit solutions seek to use conditions at both t and $t + \Delta t$ for this purpose. Those solutions also have critical numerical stability issues, but this book will deal with only the explicit solution procedures. Von Neumann and Richtmyer (1950) developed a stability analysis procedure for this problem. They used it to achieve a stable numerical solution by including additional stabilizing terms in the governing equations similar in form to viscous terms. This approach is often referred to as including artificial viscosity terms. Lax (1954) used an averaging scheme for parameters at time t to project data at $t + \Delta t$, which is equivalent to introducing artificial viscosity terms. Another approach that has been used is to apply a Taylor series expansion in time to the governing equations to extend them to second (or higher) order accuracy in time (e.g., Lax and Wendroff, 1964). Regardless of the approach used, stabilizing terms must always be added to the governing equations to achieve a stable explicit finite-difference solution. Unless extreme care is taken, these stabilizing terms can significantly influence the solution, possibly producing very unsatisfactory results. A method developed by this writer [Aungier 1970, 1971(a), 1971(b), 2000] has a definite advantage in that regard. It always permits the user of the analysis to reduce the influence of the stabilizing terms on the solution as much as necessary. But reduction of these effects is accomplished at the cost of requiring longer computation times for a steady-state solution. The method was developed by conducting a Von Neumann stability analysis on a simplified one-dimensional momentum equation to determine the minimum allowable magnitude of the stabilizing terms for a specified time step. Aungier (2000) describes this stability analysis in considerable detail. Here, only the results will be reviewed. It is convenient to represent any of the governing equations in the general form

$$u_t = v(\xi, \eta, t) + \mu^{(\xi)} u_{\xi\xi} + \mu^{(\eta)} u_{\eta\eta} \quad (5-83)$$

where the subscript notation identifies first and second partial derivatives, and the last two terms are the stabilizing terms. For a stable solution for any time step, Δt , the stability analysis shows that the coefficients of the stabilizing terms must satisfy the following conditions.

$$\mu^{(\xi)} \geq \frac{1}{2} (|W_m| + a)^2 \Delta t \quad (5-84)$$

$$\mu^{(\eta)} \geq \frac{1}{2} (|W_\theta| + a)^2 \Delta t \quad (5-85)$$

$$\mu^{(\xi)} \geq \frac{1}{2} [(|W_\xi| + a) \cos \beta]^2 \Delta t \quad (5-86)$$

$$\mu^{(\eta)} \geq \frac{1}{2} [(|W_q| + a) / \cos \beta]^2 \Delta t \quad (5-87)$$

This is satisfactory for nearly any blade-to-blade flow problem, but there are occasional exceptions when the grid structure is highly skewed and the node

spacing is much smaller in the tangential direction than in the meridional direction. The following empirical correction is applied after the meridional stabilizing term is established from Eqs. (5-84) and (5-86).

$$\mu^{(\xi)} \rightarrow \mu^{(\xi)} + \frac{1}{2} [(|W_\theta| + a) \sin^2 \beta (\Delta m) / (S \Delta \eta)]^2 \Delta t \quad (5-88)$$

So far, Δt has been treated as arbitrary, but that is really not the case. The stability analysis shows that the well-known Courant-Friedricks-Lewy (CFL) limit (Courant et al., 1928) must always be satisfied. This basically limits Δt to the time it takes for the fastest relevant characteristic wave to travel between adjacent nodes in the solution field. Thus, the maximum value of the time step allowed by the CFL limit is given by

$$\Delta t_{\max} \leq \frac{\Delta m}{|W_m| + a} \quad (5-89)$$

$$\Delta t_{\max} \leq \frac{S \Delta \eta}{|W_\theta| + a} \quad (5-90)$$

The maximum time step is computed on all time iterations by applying Eqs. (5-89) and (5-90) at all nodes in the solution field. The actual time step used is some fraction of this maximum, specified by the user.

$$\Delta t = \mu_0 \Delta t_{\max} \quad (5-91)$$

Experience has shown that the following limits should be observed to avoid numerical stability problems.

$$0.1 \leq \mu_0 \leq 0.9 \quad (5-92)$$

If the time derivative in Eq. (5-83) is approximated by a forward finite-difference approximation, the general governing equation is

$$u(\xi, \eta, t + \Delta t) = u(\xi, \eta, t) + [v(\xi, \eta, t) + \mu^{(\xi)} u_{\xi\xi} + \mu^{(\eta)} u_{\eta\eta}] \Delta t \quad (5-93)$$

But since the coefficients of the stabilizing terms are also proportional to Δt , as seen from Eqs. (5-84) through (5-88), the stabilizing terms are second order with respect to Δt , while the dynamic terms represented by the general function v are first order with respect to Δt . Hence, by simply using smaller values of Δt the influence of the stabilizing terms can be reduced. Of course, that will mean more time iterations must be processed for the solution to approach a steady state. The approach used by this writer is to start the analysis with a fairly large value of μ_0 (typically, 0.75) and steadily reduce it to some smaller value (typically, 0.25) as the solution approaches a steady state. This allows fairly large time steps to be used in the early iterations to accelerate the approach to a

steady state, but relatively small time steps when the solution is close to a steady state to reduce the effect of the stabilizing terms.

The stability analysis of Aungier (2000) produced other useful results. It shows that for points on the blade surfaces, no stabilizing term normal to the surface is required, i.e., the last term in Eq. (5-83) is omitted for blade surface points. It also shows that for $W_m > a$, and backward difference approximation for meridional partial derivatives

$$\frac{\partial u}{\partial m} = [u_{i,j} - u_{i-1,j}] / \Delta m \quad (5-94)$$

no stabilizing term in the ξ direction is required, i.e., the second term on the right-hand side of Eq. (5-83) can be omitted. A similar result is obtained for negative W_m , except a forward difference approximation is used

$$\frac{\partial u}{\partial m} = [u_{i+1,j} - u_{i,j}] / \Delta m \quad (5-95)$$

Hence, supersonic W_m with “upwind” differences requires no stabilizing term in the ξ direction. This permits special procedures to be used on partial derivatives with respect to m to improve accuracy for very high Mach number flows. This is not usually necessary for compressor applications, but can significantly improve results for the high Mach numbers often encountered in turbine blades. Basically a weighted average of forward and backward differences are employed, as follows:

$$u_m = F[u_{i+1,j} - u_{i,j}] / \Delta m + (1 - F)[u_{i,j} - u_{i-1,j}] / \Delta m \quad (5-96)$$

$$F = \left[\frac{1}{2} - \frac{2\overline{W}_m |\overline{W}_n|}{(|\overline{W}_m| + \overline{a} + ||\overline{W}_m| + \overline{a}|)^2} \right] \quad (5-97)$$

$$\overline{W}_m = \frac{1}{4} [W_m(m + \Delta m, \eta) + 2W_m(m, \eta) + W_m(m - \Delta m, \eta)] \quad (5-98)$$

$$\overline{a}_m = \frac{1}{4} [a_m(m + \Delta m, \eta) + 2a_m(m, \eta) + a_m(m - \Delta m, \eta)] \quad (5-99)$$

$$\mu^{(\xi)} \rightarrow 4\mu^{(\xi)} F(1 - F) \quad (5-100)$$

This procedure uses basic central-difference approximations and the basic stabilizing term form outlined previously when $W_m = 0$. As $|W_m| \rightarrow a$, $F \rightarrow 0$. Hence, for $|W_m| \geq a$, the solution will use an upwind difference approximation for the partial derivative, and the ξ stabilizing term will be zero. The result is that the minimum magnitude in the stabilizing terms allowed for stability is always used. It also results in faster convergence and sharper “shock capturing” when imbedded shock waves form in the flow field. For a period of time, a similar procedure was used relative to partial derivatives and stabilizing terms relative to the η direction. It was found that no significant benefit resulted for high Mach number

turbine blade problems, and the procedure occasionally slowed convergence and sometimes produced mild numerical instability. Interaction with the side boundaries and the higher probability that W_q and Q at a given node may change sign during the solution are believed to be the source of the problem. Presently, this writer uses standard central difference approximations and the basic stabilizing terms relative to the η direction.

The basic form of the stabilizing terms significantly affects their influence on the solution. The stabilizing terms should be formulated such that their magnitude is expected to be small when the flow approaches a steady state. The recommended stabilizing terms to be added to the right-hand side of Eqs. (5-72) through (5-75) and Eq. (5-77), in that order, are

$$\Phi_\rho = Sb[\mu^{(\xi)}\rho_{mm} + \mu^{(\eta)}\rho_{\eta\eta}] \quad (5-101)$$

$$\Phi_m = \mu^{(\xi)}(Sb\rho W_m)_{mm} + \mu^{(\eta)}(Sb\rho W_m)_{\eta\eta} + \Phi_\rho W_m \quad (5-102)$$

$$\Phi_\eta = Sb\rho[\mu^{(\xi)}(rC_\theta)_{mm} + \mu^{(\eta)}(rC_\theta)_{\eta\eta}]/r + \Phi_\rho W_\theta \quad (5-103)$$

$$\Phi_I = Sb\rho[\mu^{(\xi)}I_{mm} + \mu^{(\eta)}I_{\eta\eta}] + \Phi_\rho I \quad (5-104)$$

$$\Phi_\xi = \mu^{(\xi)}(Sb\rho W_\xi)_{mm} + \Phi_\rho W_\xi \quad (5-105)$$

The terms involving Φ_ρ in Eqs. (5-102) through (5-105) can be shown to be direct corrections for the known error in mass conservation caused by Φ_ρ when solving Eq. (5-72).

The numerical analysis used is a fairly straightforward finite-difference analysis applied to the grid structure illustrated in Fig. 5-3. The only subtle feature required relates to defining the side boundaries outside of the blade passages. When Eq. (5-77) is solved at the blade leading and trailing edges, the finite-difference approximation to the ξ derivative will involve the closest node outside the blade passage. Equation (5-77) is derived for nodes where $W_q = 0$. As the solution proceeds, the side boundaries outside the blade are continually readjusted such that β is equal to the local flow angle at the closest node outside the blade passage. This ensures that W_q will be zero at this node so that the difference approximation used in Eq. (5-77) will be valid. Aungier (2000) provides additional details on the numerical analysis that may be of interest to readers considering implementation of this method in a numerical analysis.

Figures 5-13 and 5-14 illustrate typical results from this time-marching method for the problems discussed previously for the potential flow solution, including comparison with that method. For the subsonic case, the time-marching solution generally shows better agreement with the experiments than does the potential flow method, particularly near the leading and trailing edges. It does show somewhat higher pressure-surface Mach numbers than either the experiment or the potential flow analysis, but agreement is considered very satisfactory. The predicted discharge flow angle is 21.1° , which is not in as good agreement with the experimental value of 25.0° as was achieved by the potential flow prediction of 24.4° . The transonic flow case shows similar trends, except that the potential flow analysis more accurately locates the point of maximum

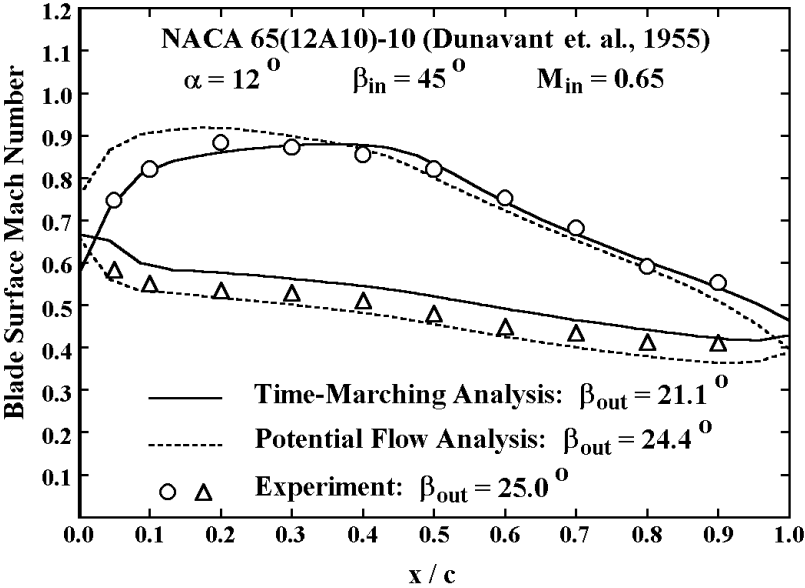


FIGURE 5-13 Time-Marching Solution Results

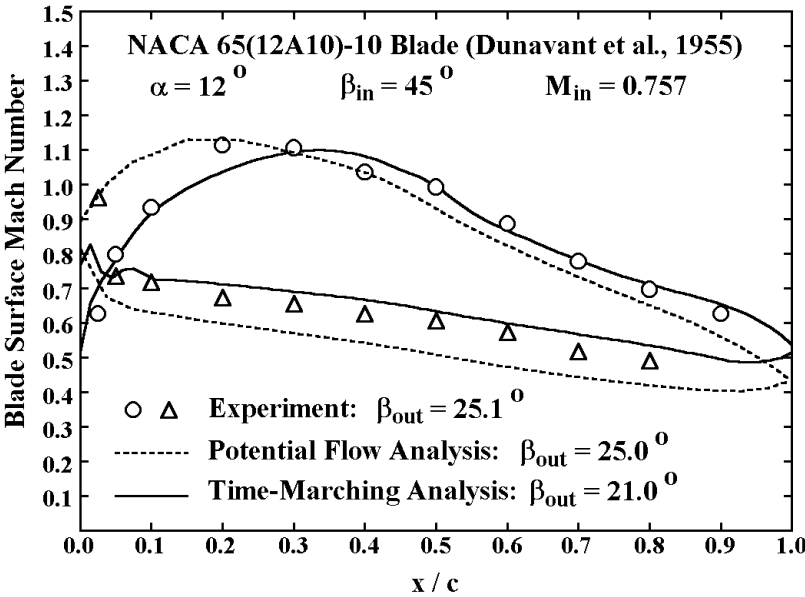


FIGURE 5-14 Transonic Time-Marching Results

Mach number. Comparison of the time-marching method with this experimental data is particularly difficult and a little misleading. This case is very close to the passage choke flow limit. The time-marching method predicts choke at a slightly lower mass flow rate than indicated by the potential flow analysis and the experiment, no doubt due to the stabilizing term influence. Indeed, the mass flow rate used in the time-marching solution is slightly lower than for the potential flow solution and the experiment. The time-marching results correspond to the lowest discharge pressure that could be assigned without causing the flow to choke, expand to supersonic velocities near the discharge and then form shock waves to adjust to the discharge pressure.

Both the potential flow and time-marching blade-to-blade flow analyses are seen to provide very useful guidance as aerodynamic design and analysis tools. For the sample problems considered, the potential flow method would be preferred due to the absence of stabilizing term effects and due to the much shorter computation time required for a solution. But the time-marching method provides a capability for solution at Mach number levels that are beyond the capability of potential flow methods.

5.6 BLADE SURFACE BOUNDARY LAYER ANALYSIS

Two-dimensional boundary layer analysis is a valuable supplement to the inviscid blade-to-blade flow analyses discussed in this chapter. This type of analysis can be added to an inviscid flow analysis with very little increase in computation time. The basic assumption of boundary layer theory is that viscous effects are confined to a thin layer close to the walls. This is usually a valid assumption for the flow in a blade-to-blade stream sheet, where the boundary layers form on the blade surfaces. However, there are usually significant pressure gradients normal to the stream sheet. Unlike the inviscid flow, the low momentum of the boundary layer fluid will be unable to balance these normal pressure gradients, causing the boundary layer fluid to migrate across stream sheets. Two-dimensional boundary layer analyses must usually be considered to be an approximation, since they neglect this effect. Yet they provide a practical and useful method to quantify viscous effects and to identify likely boundary layer separation problems. These phenomena are very important since they govern the level of total pressure loss that will occur as the flow passes through the blade row. Boundary layer analysis in turbomachinery is most conveniently accomplished by applying the equations in integral form. The basic governing equation is the momentum-integral equation derived in Chapter 3 as Eq. (3-42). In the context of the present problem, this equation can be written

$$\frac{1}{b} \frac{\partial b \rho_e W_e^2 \theta}{\partial x} + \delta^* \rho_e W_e \frac{\partial W_e}{\partial x} = \tau_w \quad (5-106)$$

The subscript e designates inviscid, boundary layer edge parameters, x is the distance along the blade surfaces and τ_w is the wall shear stress. The momentum and displacement thicknesses are defined as

$$\rho_e W_e^2 \theta = \int_0^{\delta} \rho W (W_e - W) dy \quad (5-107)$$

$$\rho_e W_e \delta^* = \int_0^{\delta} (\rho_e W_e - \rho W) dy \quad (5-108)$$

where y is the distance normal to the wall and δ is the boundary layer thickness. Usually the wall shear stress is expressed in terms of the skin friction coefficient, c_f , where

$$c_f = \frac{\tau_w}{\frac{1}{2} \rho_e W_e^2} \quad (5-109)$$

When the boundary layer initially forms on the blade, the flow will be laminar. Typically, the boundary layers on axial-flow compressor blades soon transition to turbulent flow. Hence, both laminar and turbulent boundary layer analyses are needed.

This writer prefers the laminar boundary layer analysis of Gruschwitz (1950) as reviewed by Schlichting (1968). It is a generalization of the classical incompressible Karmen-Pohlhausen solution (Pohlhausen, 1921) to compressible flow. Among other advantages, this solution allows a very direct treatment of transition to turbulence by simple application of conservation of mass and momentum. This method employs a universal boundary layer velocity profile in the form

$$W/W_e = C_1 \eta + C_2 \eta^2 + C_3 \eta^3 + C_4 \eta^4 \quad (5-110)$$

$$\eta = \frac{1}{\delta'} \int_0^y \frac{\rho}{\rho_e} dy \quad (5-111)$$

$$\delta' = \int_0^{\delta} \frac{\rho}{\rho_e} dy \quad (5-112)$$

Denoting the fluid viscosity by μ , a shape factor, Λ , is defined as

$$\Lambda = \frac{\rho_e^2}{\rho_w} \frac{(\delta')^2}{\mu} \frac{dW_e}{dx} \quad (5-113)$$

Then, by matching the boundary layer edge conditions, the coefficients in Eq. (5-110) are

$$C_1 = 2 + \Lambda/6, \quad C_2 = -\Lambda/2, \quad C_3 = \Lambda/2 - 2, \quad C_4 = 1 - \Lambda/6 \quad (5-114)$$

and the momentum thickness is given by

$$\frac{\theta}{\delta'} = \frac{37}{315} - \frac{\Lambda}{945} - \frac{\Lambda^2}{9072} \quad (5-115)$$

The boundary layer energy thickness, δ_E , and velocity thickness, δ_W , are given by

$$\frac{\delta_E}{\delta'} = \int_0^\delta \frac{\rho W}{\rho_e W_e} \left[1 - \frac{W^2}{W_e^2} \right] dy = \frac{798048 - 4656\Lambda - 758\Lambda^2 - 7\Lambda^3}{4324320} \quad (5-116)$$

$$\frac{\delta_W}{\delta'} = \int_0^\delta \left[1 - \frac{W}{W_e} \right] dy = \frac{3}{10} - \frac{\Lambda}{120} + \frac{FW_e^2}{2c_p T_e} \quad (5-117)$$

where the function F is given by

$$F = 0.232912 - 0.831483 \frac{\Lambda}{100} + 0.650584 \left[\frac{\Lambda}{100} \right]^2 + 17.8063 \left[\frac{\Lambda}{100} \right]^3 \quad (5-118)$$

For the case of adiabatic walls with the Prandtl number equal unity, the boundary layer enthalpy thickness is

$$\frac{\delta_h}{\delta'} = \int_0^\delta \frac{\rho W}{\rho_e W_e} \left[\frac{h}{h_e} - 1 \right] dy = \frac{W_e^2 \delta_E}{2c_p T_e \delta'} \quad (5-119)$$

and the displacement thickness is given by

$$\delta^* = \delta_h + \delta_W \quad (5-120)$$

Again considering adiabatic walls with the Prandtl number equal unity, the following parameters are introduced for convenience

$$b_0 = \frac{\rho_e}{\rho_w} = \frac{T_t'}{T_e} \quad (5-121)$$

$$K = \Lambda \left[\frac{\theta}{\delta'} \right]^2 = b_0 \frac{\rho_e \theta^2}{\mu} \frac{dW_e}{dx} \quad (5-122)$$

and Gruschwitz (1950) shows that

$$\frac{1}{2} c_f = \frac{\mu}{\rho_e W_e \delta'} \left[1 + \frac{\Lambda}{6} \right] \quad (5-123)$$

$$K = \left[\frac{37}{315} - \frac{\Lambda}{945} - \frac{\Lambda^2}{9072} \right]^2 \Lambda \quad (5-124)$$

The above equations are sufficient to permit numerical integration of Eq. (5-106) along x , starting at the leading edge, where $\theta = 0$, to predict θ , δ^* and δ at all other stations. In the process Gruschwitz limits the shape factor, Λ to lie in the range

$$-12 \leq \Lambda \leq 12 \quad (5-125)$$

where $\Lambda = -12$ corresponds to boundary layer separation. Normally, the boundary layer can be expected to undergo transition to turbulent flow. Many criteria for boundary layer transition have been proposed. This writer recommends use of the momentum thickness Reynolds number in the following transition criterion:

$$\text{Re}_\theta = \frac{\rho_e W_e \theta}{\mu} > 250 \quad (5-126)$$

Once the boundary layer undergoes transition to turbulent flow, different empirical relations are required to integrate Eq. (5-106). This writer prefers the entrainment method of Head (1958, 1968) as adapted by Green (1968) to compressible flows. This requires integration of the entrainment equation, presented previously as Eq. (3-44). In context of the present application, this is written as

$$\frac{\partial b \rho_e W_e (\delta - \delta^*)}{\partial x} = b \rho_e W_e E \quad (5-127)$$

The entrainment function, E , specifies the rate at which mass is entrained into the boundary layer at the boundary layer edge. To integrate Eqs. (5-106) and (5-127), empirical relations are required for E , c_f and for the various boundary layer thicknesses as a function of θ and $(\delta - \delta^*)$. Head's entrainment method was developed for incompressible boundary layers using the following shape factors as its basis:

$$H_1 \equiv (\delta - \delta^*) / \theta \quad (5-128)$$

$$H = \delta^* / \theta \quad (5-129)$$

Green (1968) recommends using a kinematic shape factor H_k in place of H when generalizing an incompressible boundary layer model to compressible flow.

$$H_k = \frac{1}{\theta} \int_0^\delta \frac{\rho}{\rho_e} \left(1 - \frac{W}{W_e} \right) dy \quad (5-130)$$

Green shows that for adiabatic walls, with the Prandtl number equal unity, H_k can be related to H by

$$H = (H_k + 1) T'_t / T_e - 1 \quad (5-131)$$

Solution of the governing equations requires empirical models for E and c_f and to relate H_k and H_l . Many alternate empirical models have been suggested for this purpose. This writer has found the following relations suitable for the present application:

$$H_k = 1 + [0.9 / (H_l - 3.3)]^{0.75} \quad (5-132)$$

$$E = 0.025(H_k - 1) \quad (5-133)$$

The skin friction coefficient correlation of Ludwig and Tillmann (1950) is commonly used for incompressible turbulent boundary layer analysis.

$$c_{f,inc} = 0.246 \exp(-1.561 H_k) \text{Re}_\theta^{-0.268} \quad (5-134)$$

Green (1968) recommends correcting this incompressible flow correlation to compressible flow by

$$c_f = c_{f,inc} H_k (H_k + 1) / [2H_k + H(H_k - 1)] \quad (5-135)$$

These empirical relations are sufficient to integrate Eqs. (5-106) and (5-127), starting at the transition point. At the transition point, the mass and momentum flow in the turbulent boundary layer must match the values computed for the laminar boundary layer. From Eqs. (3-35) and (3-38), this requires

$$(\delta - \delta^*)_{turb} = (\delta - \delta^*)_{lam} \quad (5-136)$$

$$\theta_{turb} = \theta_{lam} \quad (5-137)$$

From the Gruschwitz (1950) profiles, it can easily be shown that

$$\delta - \delta^* = \delta' \left[\frac{7}{10} + \frac{\Lambda}{120} \right] \quad (5-138)$$

Equation (5-137) is normally applied at the transition point, along with some assumption on how H changes during transition from laminar to turbulent flow. Use of the Gruschwitz laminar boundary layer model permits a more fundamental method based on conservation of mass and momentum. This writer uses $H_k \geq 2.4$ as a separation criterion for turbulent boundary layers. During the analysis, the kinematic shape factor is limited to this value to avoid solution divergence and permit the analysis to continue through a separation zone. This is necessary, since it is not uncommon for the boundary layer to reattach, particularly on the pressure surface of the blade.

When boundary layers on the blade surfaces have been computed, it is useful to predict the total pressure loss coefficient for the cascade from the boundary layer data at the trailing edge. Following Lieblein and Roudebush (1956), the

total pressure loss coefficient based on the cascade inlet velocity pressure can be approximated by

$$\bar{\omega} = \frac{\Delta P_t}{(P_t - P)_{in}} = \left(\frac{\cos \beta_{in}}{\cos \beta_{out}} \right)^2 \frac{2\Theta + (\Delta^*)^2}{(1 - \Delta^*)^2} \quad (5-139)$$

$$\Theta = \frac{\sum \theta}{S \cos \beta_{out}} \quad (5-140)$$

$$\Delta^* = \frac{\sum \delta^*}{S \cos \beta_{out}} \quad (5-141)$$

where the summations are carried out for the boundary layers on both blade surfaces at the blade trailing edge. In the case of rotor blade rows, this total pressure loss coefficient can also be used to estimate the rotor efficiency via the methods described in Chapter 2. Equation (5-139) is derived directly from conservation of mass and momentum, at the blade trailing edge, while assuming that the low momentum boundary layer fluid instantly mixes with the inviscid free stream fluid while the static pressure remains constant. Those readers who completed Exercise 3.6 have, in fact, already derived a simple incompressible form of this equation under the same assumptions.

Loss coefficients computed from two-dimensional boundary layer predictions should be regarded as quite approximate. The analysis ignores secondary flow effects associated with boundary layer migration normal to the stream sheets, which are often quite significant in an annular cascade within an axial flow compressor. Also, the boundary layers are often predicted to separate at some point along the blade surface. The basic assumptions of boundary layer theory are not satisfied in separation zones, causing the predictions to be of questionable accuracy. It can be expected that the loss coefficient in an annular cascade of an axial-flow compressor will be significantly higher than is predicted by Eq. (5-139). Loss coefficients calculated in this fashion do have qualitative significance to guide the designer in evaluation of relative differences in loss for alternative cascade designs.

Figure 5-15 shows predicted boundary layer shape factors, H , of Eq. (5-129) that are generated by a two-dimensional boundary layer analysis conducted using results from the inviscid potential flow analysis results as the boundary layer edge conditions. The inviscid flow blade-loading diagram for the case considered is shown in Fig. 5-6. Transition from laminar to turbulent flow occurs close to the leading edge for both blade surfaces. The deceleration of the inviscid velocity on the suction surface is severe enough to lead to a significant boundary layer separation zone starting well upstream of the blade trailing edge. As noted in the discussion of Fig. 5-6, the experimental data appears consistent with the premise that boundary layer separation may have occurred in this region.

Numerical analysis for the two-dimensional boundary layer is relatively straightforward. The governing equations are parabolic in mathematical form. Hence, a simple marching type solution is needed, since the solution at each streamwise station depends only on the upstream boundary layer parameters.

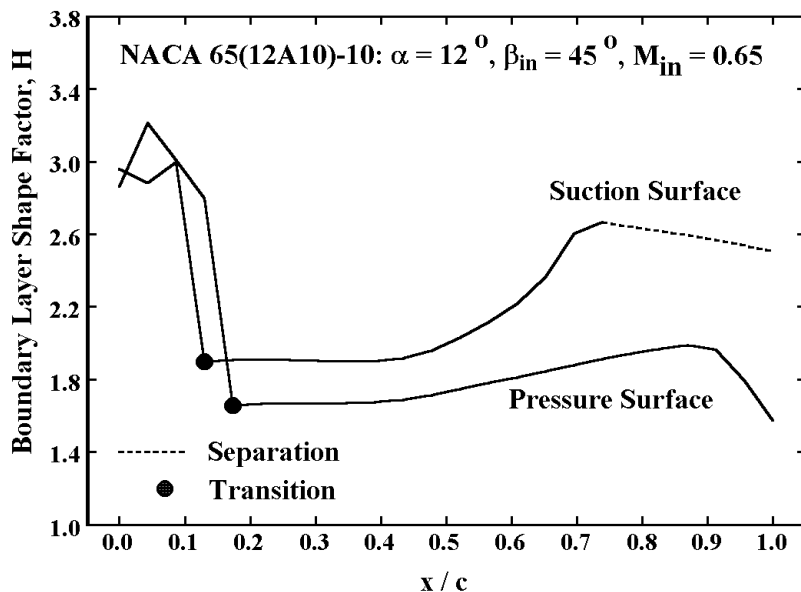


FIGURE 5-15 Boundary Layer Analysis Result

Streamwise derivatives in the governing equations are replaced with backward-difference approximations of the form of Eq. (5-94). An iterative solution procedure is used to complete the integration of the governing equations at each streamwise station before proceeding to the next station. Aungier (2000) outlines the procedure used by this writer. In this book, the outline of a numerical procedure is left as an exercise for the interested reader, with appropriate guidance provided in the exercises.

5.7 SUMMARY

The analysis methods described in this chapter are representative of available theoretical methods for predicting the two-dimensional flow in cascades. There are many alternate solution techniques in use, both for the inviscid flow and the boundary layer. But the precise technique used is less significant than the approximations that are inherent in the two-dimensional flow model. It has been seen that reasonable estimates of the fluid turning can be achieved, but reasonable estimates are not good enough when errors are compounded in a multistage compressor analysis. The limitations relative to loss prediction have been discussed in the previous section. These theoretical methods suffer from a more fundamental limitation that has not yet been discussed. Both the inviscid flow and the boundary layer analyses suffer a dramatic loss of accuracy when applied under far off-design conditions, where severe flow separation may exist. Indeed,

there is very little merit in even applying them to such cases, yet these situations must be addressed when analyzing a compressor.

Faced with this problem, design engineers normally turn to empirical models or seek a more fundamental analysis technique. Empirical modeling of cascade performance has a very long history in axial-flow compressor aerodynamic technology. Supported by extensive cascade testing, particularly by the NACA, rather accurate empirical models are available. These empirical models play such an essential role in axial-flow compressor aerodynamic design and analysis that they are covered in some detail in Chapter 6. Use of more fundamental theoretical methods is also receiving much attention. One well-established extension of the methods in this chapter is to combine them with a hub-to-shroud flow two-dimensional flow analysis to form a quasi-three-dimensional flow analysis. Through interaction between the two analyses, it is possible to identify the stream sheet geometry, which has simply been treated as a known quantity in this chapter. In the case of centrifugal compressor aerodynamic design and analysis, the quasi-three-dimensional flow model plays an essential role (Aungier, 2000). Its advantages for axial-flow compressors are far less dramatic, but sufficient to warrant presenting the technique in Chapter 12 of this book. The more fundamental advance in theoretical analysis is the use of viscous flow computational fluid dynamics (CFD) codes. The design engineer will typically employ one of several commercially available CFD codes that are well suited to turbomachinery applications. Viscous CFD offers considerable promise for removing most of the limitations of the methods described in this chapter. Indeed, it has already greatly alleviated many of them, although much remains to be done in the areas of turbulence modeling, numerical methods and computational speed before these methods can be considered exact. Viscous CFD is occasionally applied to the two-dimensional blade-to-blade flow problem, but its real merit lies in treating the fully three-dimensional flow problem, where the important secondary flow patterns are also modeled. At present, the primary role of viscous CFD is in the area of advanced blade or stage design where its more fundamental fluid dynamics models can be used to advantage for reducing losses and increasing the operating range within practical computer running times.

EXERCISES

- 5.1 Derive an alternate expression for Eq. (5-10) by expressing the partial derivatives with respect to m and θ in terms partial derivatives with respect to ξ and η and substituting them into Eq. (3-21). Reduce this alternate continuity equation to a finite-difference form using central-difference approximations similar in form to Eqs. (5-40) and (5-41). Simplify this difference equation to a mass balance equation for the control volume of Fig. 5-4, and show that the mass balance achieved for a numerical analysis by this alternate derivation is less accurate than that given by Eq. (5-8).
- 5.2 Develop Taylor series expansions about the meridional coordinate position, m , for $\psi(m+\Delta m)$ and $\psi(m-\Delta m)$ in terms of $\psi(m)$ and its derivatives. Use these relations to derive Eqs. (5-35) and (5-37).

Express the order of accuracy of these finite-difference approximations in terms of Δm .

- 5.3 Develop Taylor series expansions about the meridional coordinate position, m , for $\psi(m+\Delta m)$ and $\psi(m+2\Delta m)$ in terms of $\psi(m)$ and its derivatives. Use these relations to derive Eq. (5-40). Express the order of accuracy of this finite-difference approximation in terms of Δm .
- 5.4 From a truncated Taylor series expansion about the meridional coordinate position, m , for $u(m+\Delta m)$, derive Eq. (5-95). Express the order of accuracy of this finite-difference approximation in terms of Δm .
- 5.5 The paragraph preceding Eq. (5-101) notes that the form of the stabilizing terms used in a time-marching solution is an important consideration. Consider flow in the portion of the solution domain upstream of the blade where the flow is uniform on the upstream boundary. Comment on the expected magnitudes of the stabilizing terms associated with $\mu^{(5)}$ in Eqs. (5-102) through (5-104) when the flow is approximately steady state. Why is the term $Sb\rho$ outside of the partial derivative in Eqs. (5-103) and (5-104) but inside the partial derivative in Eq. (5-102)? If the form of the stabilizing terms causes them to be very small in magnitude near a steady state, how can they stabilize the numerical analysis?
- 5.6 Consider the numerical solution of the laminar boundary layer equations at a specific streamwise station where all boundary layer edge conditions and all boundary layer parameters at the upstream station are known.
 - (a) Define a procedure to estimate a “safe” initial guess for θ at the current station from the upstream station, which accounts for change in just boundary layer edge conditions. Suggest a “safe” procedure for the case where the upstream station is the leading edge.
 - (b) Outline a procedure that might be followed to predict the laminar boundary at this station in terms of specific steps [parameter to predict and equation number(s) to be used]. It is understood that these steps will be repeated, in order, until the process converges.
- 5.7 Repeat Exercise 5.6 for turbulent boundary layers, except that in this case the upstream station cannot be the leading edge, so that issue is not relevant.